Macromolecules
ARTICLE

Macromolecules **2009**, *42*, 8343–8352 **8343**
DOI: 10.1021/ma901565h

Poly(ethylene oxide) Crystal Orientation Change under 1D Nanoscale Confinement using Polystyrene-*block*-poly(ethylene oxide) Copolymers: Confined Dimension and Reduced Tethering Density Effects

Ming-Siao Hsiao,[†] Joseph X. Zheng,[†] Ryan M. Van Horn,[†] Roderic P. Quirk,[†] Edwin L. Thomas,[‡] Hsin-Lung Chen,[§] Bernard Lotz,[∥] and Stephen Z. D. Cheng*,[†]

[†]*Maurice Morton Institute and Department of Polymer Science, The University of Akron, Akron, Ohio 44325-3909,* [‡]*Department of Materials Science and Engineering, Massachusetts Institute and Technology, Cambridge, Massachusetts 02139,* [§]*Department of Chemical Engineering, National Tsinghua University, Hsinchu, Taiwan 300, ROC, and* [∥]*Institut Charles Sadron, 23, Rue du Loess, Strasbourg 67034, France*

Received July 17, 2009; Revised Manuscript Received September 6, 2009

ABSTRACT: In this study, we systematically investigated the effects of confined dimension (the thickness of PEO layer) and reduced tethering density ($\tilde{\sigma}^{PEO}$, defined by $\sigma\pi R_g^2$, where σ is the tethered chain density and R_g is the radius of gyration of the tethered PEO chain in its end-free state in the melt) on the PEO crystal orientation change within a 1D nanoscale confinement. We realized this confinement by utilizing two symmetric polystyrene-*block*-poly(ethylene oxide) (PS-*b*-PEO) diblock copolymer single crystals grown at different crystallization temperatures (T_x) in dilute solution via the self-seeding technique. After these single crystals were collected as mats, the thicknesses of both the PEO single crystal (d_{PEO}) and PS glassy layer were measured using small-angle X-ray scattering (SAXS) coupled to the 1D correlation function. Because T_g^{PS} is higher than T_m^{PEO} in those PS-*b*-PEO single crystal mats, 1D confinements having different d_{PEO} and $\tilde{\sigma}^{PEO}$ values can be prepared by changing T_x values. The PEO block single crystals were melted and recrystallized at different temperatures (T_{rx}), and the *c*-axis orientation of the recrystallized PEO crystals with respect to glassy PS layers at different T_{rx} values can be monitored by simultaneous 2D SAXS and WAXD techniques. Two observations of the PEO crystal orientation were found in these PS-*b*-PEO mats. First, three different *c*-axis orientations of the PEO crystals with respect to the PS layer normal were observed: random, homogeneous, and approximately homeotropic. Second, a dramatic change from homogeneous to homeotropic takes place within a few degrees Celsius. The onset temperature of this orientation change (T_{onset}) decreases with increasing d_{PEO} and $\tilde{\sigma}^{PEO}$ values. The T_{onset} values were found to lie within a temperature range of nearly 20 °C (from 0 to −19 °C). Mechanisms of the confined dimension and reduced tethering density effects on determining those T_{onset} values are proposed.

Introduction

Confined crystallization utilizing crystalline-*block*-amorphous diblock copolymers as templates has received much attention over the past decade because the crystallization of the crystalline blocks in different nanoscale confinement (1D, 2D, or 3D) exhibits significantly different behaviors compared with that of crystalline polymer in the bulk.[1−30] In the construction of hard confinement environments using these diblock copolymers, the three major structural formation processes are required to follow the temperature sequence where the order−disorder transition temperature (T_{ODT}) is higher than the glass-transition temperature of the amorphous block ($T_g^{am.}$) and where both are higher than the melting point of the crystalline block ($T_m^{cryst.}$).[20]

The simplest confinement is a 1D lamellar environment. This can be achieved by utilizing large amplitude shear on a crystalline-*block*-amorphous diblock copolymer bulk sample with the two components having symmetric volume fractions. Crystallization kinetics and crystal orientation with respect to the confined glassy layer normal in this confinement are the two most studied properties. Sheared polystyrene-*block*-poly(ethylene oxide) (PS-*b*-PEO) diblock copolymers have been serving as the template for the systematic study of these two issues for a decade.[21,22,26,31−35] However, this approach has some problems because the confined structures generated in the bulk using mechanical shearing inevitably contain defects such as edge and screw dislocations. The existence of defects releases the confinement and affects the crystallization kinetics.[31] The PEO crystal orientation (usually, it is represented by the *c*-axis orientation) in this system can be tailored by the control of crystallization temperature (T_x) and confined size.[21,26] Furthermore, the initial step of crystal growth determines the final crystal orientation.[22]

To avoid the structural defects associated with bulk samples under mechanical shearing, we have very recently adopted a new approach by utilizing PS-*b*-PEO single crystals grown in solution and their subsequent single crystal mats as templates.[36,37] In this case, PS-*b*-PEO single crystals have a "sandwich-like" lamellar structure composed of a PEO single crystal layer and two PS layers covering both of the PEO single crystal basal surfaces. Therefore, no structural defects or interconnection between individual single crystal layers exists. Because the T_g^{PS} of the both layers is higher than the T_m^{PEO} of the single crystal, a 1D hard confinement is created for investigating the crystallization and orientation changes of the PEO blocks after the PEO single crystals were melted and recrystallized at different temperatures (T_{rx}).[37]

*To whom correspondence should be addressed. E-mail: scheng@uakron.edu.

© 2009 American Chemical Society

Published on Web 09/21/2009

Table 1. Molecular Weights and T_{ODT} Values of PS-*b*-PEO Samples Used in This Study

PS-*b*-PEO	$\overline{M}_n^{PS}$ (g/mol)	$\overline{M}_n^{PEO}$	f_{PEO}	T_{ODT} (°C)[a]
61k-*b*-57k	61 300	57 000	0.468	> 200
26k-*b*-23k	26 100	23 100	0.456	190

[a] T_{ODT} was measured from temperature-dependent 1D SAXS curves of the PS-*b*-PEO diblock copolymers.

On the basis of our electron diffraction (ED) and simultaneous 2D small angle and wide-angle X-ray scattering (SAXS and WAXD) results, it has been observed that first, the crystallization of the PEO blocks cannot take place until the T_{rx} enters the homogeneous nucleation region,[36] and second, the sharp change of the *c*-axis orientation from perpendicular to parallel to the PS layer normal occurs within a few degrees Celsius.[37] The question still remains of whether this orientation change is dependent on confined volume, 1D confined thickness (d_{PEO}), and/or reduced tethering density ($\tilde{\sigma}^{PEO}$)[38,39] of the PEO blocks between the PS solid layers. In this study, we designed experiments to generate a series of PS-*b*-PEO single crystals with different confined volume, d_{PEO}, and $\tilde{\sigma}^{PEO}$ values to seek quantitative answers for these dependencies.

Experimental Section

Materials and Samples. Two PS-*b*-PEO diblock copolymers having different molecular weight and composition were used in this study. The detailed sequential living anionic polymerization of the sample was described elsewhere.[40] The M_n^{PS} precursors were synthesized first, and their polydispersities were characterized by size exclusion chromatography (SEC) using polystyrene standards. The M_n^{PEO} blocks were then polymerized from the PS precursors, and their molecular weights were determined by proton nuclear magnetic resonance spectroscopy (^{1}H NMR). The polydispersity in the final diblock copolymers was measured by SEC using the universal calibration. The molecular weight characterization and the volume fraction of PEO blocks as well as the order-to-disorder transition temperature (T_{ODT}) in the melt of these two samples are listed in Table 1.

We prepared 10 different solutions of PS-*b*-PEO single crystals by varying T_x in solution crystallization, including 5 from 61k-*b*-57k PS-*b*-PEO and 5 from 26k-*b*-23k PS-*b*-PEO, with different PEO single crystal thicknesses (d_{PEO}) and reduced tethering densities of the PEO block ($\tilde{\sigma}^{PEO}$). The single crystal preparation of the PS-*b*-PEO sample was described in previous articles.[36−39,41,42] Growing large amounts of uniform, large size PS-*b*-PEO single crystals is a prerequisite for preparing single crystal mats. In this study, large populations of PS-*b*-PEO single crystals were carried out in a mixed solvent of chlorobenzene and octane with a 1:1 weight ratio under dilute solution conditions (0.05 wt % polymer). Solvents used here were HPLC grade, dried with CaH_2, and freshly distilled. The PS-*b*-PEO samples were dissolved above T_d = 42 °C in a temperature-controlled oil bath. The self-seeding procedure was utilized to achieve a large number of single crystals with a uniform size.[41,43] The homogeneous polymer solution was crystallized at room temperature overnight and reheated to a seeding temperature 1 °C lower than the T_d and kept there for 20 min. The sample was then quenched to a preset T_x in an isothermal oil bath to grow single crystals. The preset T_x value was set at 20, 24, 29, 34, or 37 °C to obtain different d_{PEO} and $\tilde{\sigma}^{PEO}$. Note that only lamellar single crystals with uniform sizes were formed in the solutions of the PS-*b*-PEO samples.

Single crystal suspensions in the solution were filtered utilizing the design from our laboratory following the procedure published in refs 44 and 45. The single crystals were filtered and washed twice by the mixed solvent. Then, the solution was quenched in excess ethyl benzene.[41,46] Note that ethyl benzene is a poor solvent for both PS and PEO, and the PS blocks were vitrified via quenching during precipitation of the single crystals. We carefully collected 10 different sets of PS-*b*-PEO single crystals at the bottom of their respective test tubes. Finally, each set was dried in a vacuum oven at room temperature for 3 days to obtain single crystal mats. A typical single crystal mat size was 1.0×1.0×1.0 mm^3. These sample sizes ensured that they could be free-standing during the SAXS and WAXD measurements without any substrate support. ^{1}H NMR and SEC experiments were performed on the mat samples prepared by redissolving the PS-*b*-PEO single crystals. No changes in molecular weights, molecular weight distributions, or PEO composition were observed, suggesting that there is no molecular fractionation during the PEO block crystallization in dilute solution.

Equipment and Experiments. Differential scanning calorimetry (DSC) experiments were carried out on a Perkin-Elmer PYRIS Diamond DSC with an Intracooler 2P apparatus to measure the T_m^{PEO} of the PEO layer and the T_g^{PS} of the PS layer in the PS-*b*-PEO single crystal mats. The fully crystallized single crystal mats with a typical weight of 1.0 mg were heated at 10 °C/min. The endothermic peak temperature was taken as the T_m^{PEO}. The weight-percent crystallinity was calculated using an equilibrium heat of fusion for PEO crystals (8.66 kJ/mol)[47] and was normalized to the PEO weight fraction in the PS-*b*-PEO samples. T_g^{PS} was identified as the midpoint of the stepwise increase in the heat capacity.

The PS-*b*-PEO single crystal images were captured from an Olympus BH-2 phase contrast optical microscopy (PCOM). The scale bar was calibrated in both lateral and vertical directions using the standard grid. A typical scale bar was 20 μm.

We carried out the recrystallization process by first heating the single crystal samples to the melting temperature at the end of the DSC measurement peak and keeping them there for 4 min. Note that different thicknesses of the PEO lamellar crystals possessed different melting temperatures. The samples were then quenched to a preset T_{rx} for recrystallization of the PEO blocks. When the T_{rx} is above −10 °C, the sample temperatures for melting the original PEO crystals were slightly reduced, about 0.2 °C, to have a few seeds for recrystallization. The determination of these reduced temperatures was carefully checked to make sure that the remaining seeds would not affect the crystal orientation of the recrystallized PEO crystals.[22]

Simultaneous 2D SAXS and WAXD experiments were performed using a Rigaku SAXS and WAXD instrument with an 18 kW rotating anode X-ray generator (MicroMax-002$^+$) equipped with a Cu tube operated at 45 kV and 0.88 mA. The wavelength of the X-ray beam was 0.15418 nm. The zero pixel of the 2D SAXS patterns was calibrated using silver behenate with the first-order scattering vector, q, being 1.076 nm^{-1}. ($q = 4\pi \sin\theta/\lambda$, where λ is the wavelength and 2θ is the scattering angle.) 2D WAXD patterns were calibrated using α-Al_2O_3 with known crystal diffraction at $2\theta = 28.47°$. An exposure time of 15 min is required to obtain a high-quality SAXS diffraction pattern.

2D WAXD experiments were also conducted using an imaging system (Rigaku, R-AXIS-IV) with an 18 kW rotating anode X-ray generator. The received patterns were calibrated via the same procedure as that in simultaneous X-ray experiments. A 2 h exposure time was required for obtaining a high-quality WAXD pattern. In all 2D X-ray experiments, background scattering was subtracted from the sample scans.

The 1D correlation function ($\gamma(z)$) of lamellar PS-*b*-PEO single crystals in real space derived from the Fourier transform of the 1D SAXS profiles ($I(q)$ versus q) is introduced here for precisely evaluating the individual thickness of the PEO single crystal, the glassy PS layer, and the overall long period ($L = d_{PEO} + 2d_{PS}$). The 1D correlation function is defined as

$$\gamma(z) = \frac{1}{\gamma(0)} \int_0^\infty I(q) q^2 \cos(qz)\, dq \qquad (1)$$

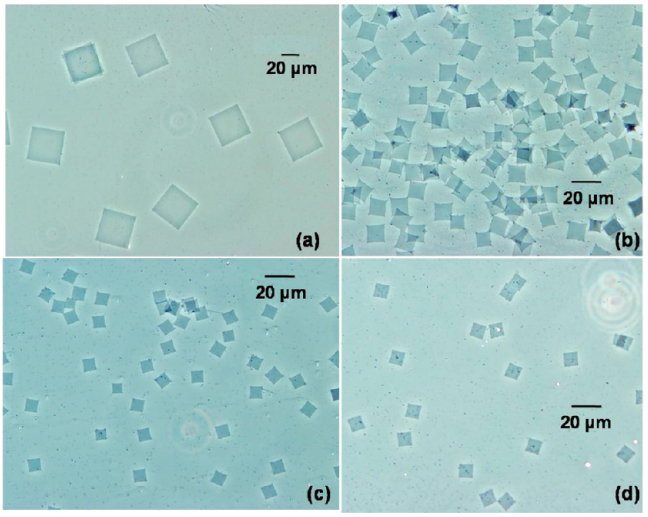

Figure 1. Phase contrast optical microscopy (PCOM) images of PS-*b*-PEO diblock copolymer single crystals (61k-*b*-57k) grown in mixed chlorobenzene/octane solvent at solution crystallization temperature, T_x, of (a) 24, (b) 29, (c) 34, and (d) 37 °C.

where z is the direction along which the electron density is measured and $\gamma(0)$ is just the scattering invariant

$$\gamma(0) = \int_0^\infty I(q)q^2 \, dq \qquad (2)$$

Because of the finite q range of experimental SAXS data, extrapolation of the 1D azimuthal scan SAXS data to both the low and high q region is necessary for the integration of the intensity, $I(q)$. Extrapolation to $q(0)$ was achieved by linear extrapolation, and extension of the intensity to large q values can be accomplished by using the Porod−Ruland model.[48−51] The 1D correlation function is measured after subtracting the background intensity arising from thermal density fluctuations from the overall intensity. The position of the first maximum determines the long period value (L), and the intersection of the baseline with the straight line extended from the self-correlation triangle was measured as the thinner layer thickness or the PEO layer thickness of the sandwiched lamellae of the PS-*b*-PEO single crystal.[52]

Results and Discussion

Structure and Property Parameters and Tethering Densities for Two Series of PS-*b*-PEO Single Crystal Mats. Figure 1a−d shows a series of PCOM images that contain large amounts of square PS-*b*-PEO (61k-*b*-57k) single crystals grown in chlorobenzene/octane mixed solvent at different T_x values ranging from 24 to 37 °C. These square crystals are bounded by four (120) crystallographic planes. The sizes of the PS-*b*-PEO single crystals grown at different T_x values are uniform, and the lateral sizes are on the micrometer scale because of the self-seeding procedure. As reported in our previous publications, glassy PS blocks completely cover the top and bottom basal surfaces of the PEO single crystal.[36−39,42] Therefore, these square PS-*b*-PEO single crystals possess a "sandwich-like" lamellar structure.

The thermodynamic properties of the two series of PS-*b*-PEO mats grown at different T_x values were measured by DSC. For the PS-*b*-PEO (61k-*b*-57k) single crystal mats grown at T_x = 29 °C as an example (sample ID is 61k-*b*-57k/3), a T_m^{PEO} of 60.0 °C is observed. (Because similar DSC diagrams have been shown in our previous publications,[36,37] it is not included here.) The T_m^{PEO} values of the other four PEO single crystal mats of the PS-*b*-PEO (61k-*b*-57k) range from 58 to 62 °C as a function of T_x. Meanwhile, a weak T_g^{PS} transition region above the T_m^{PEO} region can be observed in the DSC thermal diagrams. These T_m^{PEO} values were determined at a heating rate of 10 °C/min. The slower heating rates could generate even lower T_m^{PEO} values under a condition that the metastability of these crystals are not changed during heating[53] because of the confinement generated by two glassy PS layers on the top and bottom of the PEO single crystals.

Table 2. Structural Parameters, Tethering Densities, and the Onset Temperature of Crystal Orientation Change for Two PS-*b*-PEO Single Crystal Mats with Different Molecular Weights and Compositions[a]

sample ID	T_x (°C)	d_{PS} (nm)	d_{PEO} (nm)	σ (nm^{-2})	$\tilde{\sigma}^{PEO}$	T_{onset}
61k-*b*-57k/1	20	5.0	9.4	0.052	13.6	0
61k-*b*-57k/2	24	5.7	10.4	0.058	15.4	−4
61k-*b*-57k/3	29	6.0	11.4	0.062	16.4	−10
61k-*b*-57k/4	34	6.8	12.7	0.070	18.4	−16
61k-*b*-57k/5	37	7.4	13.8	0.076	20.2	−20
26k-*b*-23k/1	20	5.1	9.0	0.121	13.0	−1
26k-*b*-23k/2	24	5.8	10.4	0.141	15.0	−5
26k-*b*-23k/3	29	6.5	11.6	0.158	16.8	−9
26k-*b*-23k/4	34	7.6	13.4	0.184	19.7	−16
26k-*b*-23k/5	37	8.4	14.4	0.204	21.8	−19

[a] Two PS-*b*-PEO single crystals grown at T_x ranging from 20 to 37 °C in dilute solution

We calculated crystallinity values of these two series of samples by measuring the heats of fusion of the endothermic peaks and comparing them with the equilibrium heat of fusion. All of the calculated crystallinity values of the single crystal samples are above 95%. For the recrystallized PEO mat samples, their crystallinity in the low T_{rx} region where no self-seeding procedure is required was around 20−30%. In the high T_{rx} region where the self-seeding procedure is necessary, the values of these recrystallized PEO crystals were > 50%.

The upper-limit temperature of the vitrified PS layer in the mats held in the solid state can be precisely determined by utilizing temperature-dependent 2D SAXS. Figure 2a−e shows a set of 2D SAXS patterns along the direction perpendicular to the lamellar normal (the z-direction, as shown in the inset of the Figure) obtained during heating of the mats at different temperatures for PS-*b*-PEO (61k-*b*-57k) single crystal mats collected after crystallizing at T_x = 29 °C. It is evident that up to five orders of the diffraction peaks can be clearly identified, and the d-spacing (or long period value) is determined to be 23.4 nm. The azimuthal scans of Figure 2a−e generate a set of 1D SAXS diagrams, as shown in Figure 2f. These scattering curves have the peak ratio of 1:3:5. The extinction of even order scattering peaks may be attributed to the high symmetry of this sandwiched lamellar structure. These results show that the stacked sandwiched lamellae possess a long-range, 1D layer-orientation order along the normal direction (the z-direction). The overall layer thickness (or long period, $L = d_{total} = d_{PEO} + 2d_{PS}$) calculated from the q^{max} value of the first peak in those SAXS data is 23.4 nm. Figure 2g shows the relationship between the L values and temperatures. Upon increasing the temperature, the measured layer thickness exhibits a sudden increase from 23.4 to 49.8 nm as soon as 85 °C is reached. This evidence proves that the PS blocks can no longer hold the thin layers in the vitrified state, and the PS-*b*-PEO copolymer returns to the equilibrium heterogeneous melt with a larger lamellar layer thickness in the bulk. This temperature is thus recognized precisely as the upper-limit temperature for the PS-*b*-PEO (61k-*b*-57k) single crystal mats at T_x = 29 °C. The T_g^{PS} values of the PS-*b*-PEO single

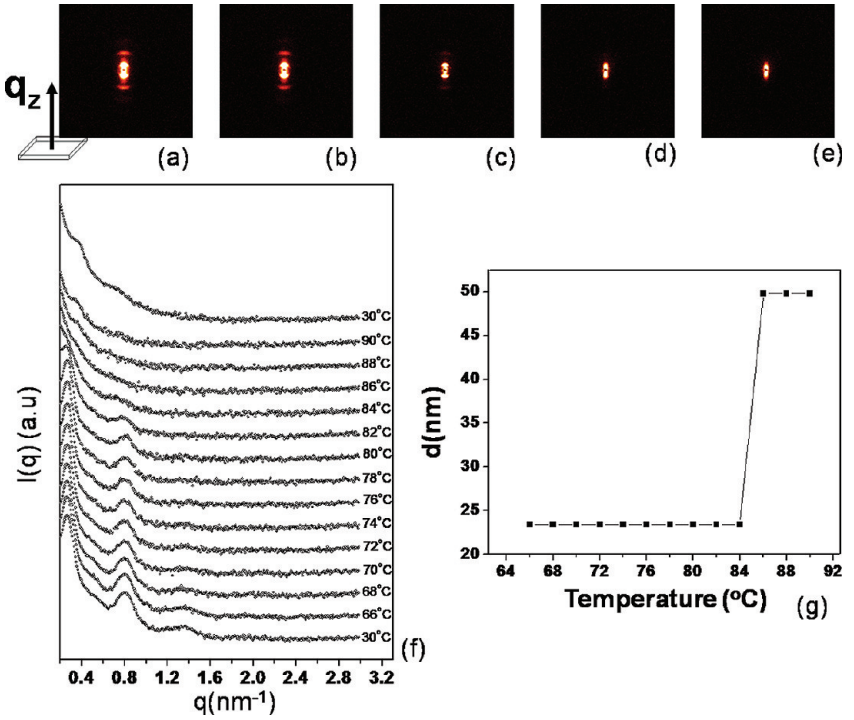

Figure 2. Series of 2D SAXS patterns of PS-*b*-PEO single crystal mats (61k-*b*-57k) grown at $T_x = 29$ °C in chlorobenzene/octane solvent taken from different temperatures during the heating process ($T = 75$, 80, 82, 84, and 86 °C from left to right (a−e)) when the X-ray is along *x*,*y*-plane. (f) Corresponding azimuthal scan integrated 1D SAXS curves. (g) The sudden change in the value of the long period (*d*-spacing) of PS-*b*-PEO diblock copolymer mats at 85 °C represents the glass transition temperature (T_g^{PS}) of thin glassy PS layers.

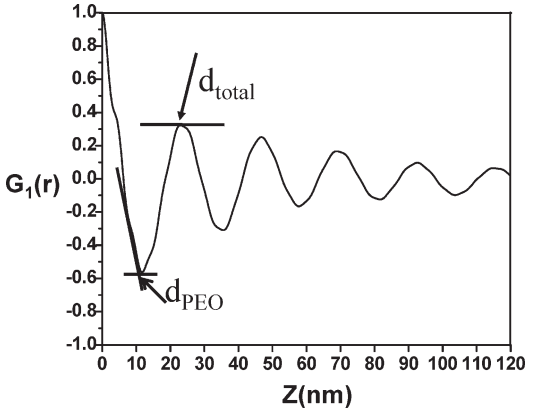

Figure 3. 1D correlation function of PS-*b*-PEO diblock copolymer single crystal mats at $T_x = 29$ °C (61k-*b*-57k) calculated from the azimuthal scan 1D SAXS profile.

crystal mats collected at different T_x values are all higher than 80 °C for the case of the PS-*b*-PEO (61k-*b*-57k) and higher than 64 °C for the PS-*b*-PEO (26k-*b*-23k) single crystal mats, as confirmed by the temperature-dependent SAXS experiments. The differences between the T_g^{PS} and T_m^{PEO} values in these PS-*b*-PEO mats provide a window to melt the PEO single crystals and recrystallize them in the 1D confined environment for investigating the roles of d_{PEO} and $\tilde{\sigma}^{PEO}$ on the *c*-axis orientation change with respect to the PS layer normal in the recrystallized PEO crystals at different T_{rx} values.

To verify the thickness of each individual PEO single crystal and top and bottom PS layers in the mats, we used the 1D correlation function. Figure 3 is a 1D correlation function of the PS-*b*-PEO single crystal mats collected at $T_x = 29$ °C (61k-*b*-57k) as an example. The position of the first maximum represents the average thickness d_{total}, and this d_{total} value calculated from the SAXS scattering peak was considered to be the weight-average value.[52,54] The intersection of the baseline and straight line extended from the self-correlation triangle corresponds to the average thickness of the thinner layer. This value is considered to be the thickness of the PEO layer (d_{PEO}) because the weight fraction of PEO blocks is < 0.5 in this PS-*b*-PEO sample (61k-*b*-57k). The values of d_{PS} and d_{PEO} in the series of PS-*b*-PEO single crystal mats can be individually deduced using their corresponding 1D correlation functions. Figure 4a shows the relationship between d_{PEO} and T_x for the ten PS-*b*-PEO single crystal mats samples with different molecular weights (61k-*b*-57k and 26k-*b*-23k) grown and collected at different T_x, ranging from 20 to 37 °C in the mixed solvent.

In Figure 4a, the d_{PEO} values of the two PS-*b*-PEO samples slightly increase with T_x in the whole T_x region studied, and the relationship between d_{PEO} and T_x in these two PS-*b*-PEO mats is similar. No sudden change of the d_{PEO} values was found in the T_x regions studied. A clearer presentation can be seen when plotting the relationship between $1/d_{PEO}$ and T_x, as shown in Figure 4b. These linear relationships indicate that the lamellar thicknesses of these single crystals fit the modified Thomson−Gibbs equation with extra-surface free energy attributed by the entropic interactions generated from crowding of the amorphous PS blocks, as discussed in ref 39.

The values of the reduced tethering density of the PS blocks on the PEO single crystal substrates ($\tilde{\sigma}^{PS}$) at different T_x values were calculated according to $\tilde{\sigma}^{PS} = (1/S)\pi(R_g^{PS})^2$, where S is the surface area for a single tethered PS block and R_g^{PS} is the radius of gyration of the PS block. These S values can be calculated by $S = M_n^{PS}/(N_A \times \rho_{PS} \times d_{PS})$ in units of square nanometers per chain. Here M_n^{PS} is the number-average molecular weight of the PS block, N_A is Avogadro's number, ρ_{PS} is the density of the PS block (1.052 g/cm^3), and d_{PS} is the thickness of the PS layer. In the case of PS-*b*-PEO

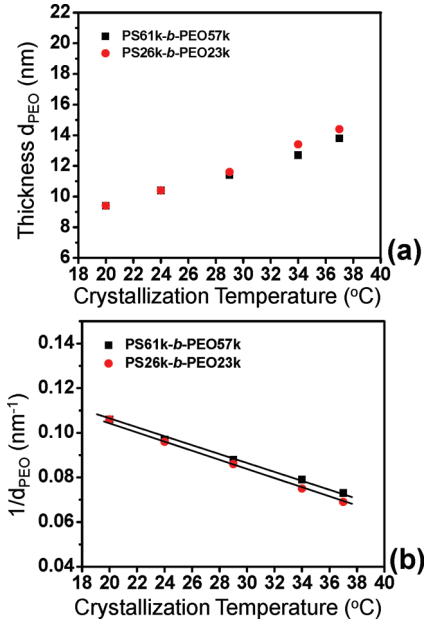

Figure 4. (a) Relationships of d_{PEO} and T_x and (b) relationships of $1/d_{PEO}$ and T_x for the two symmetric PS-*b*-PEO diblock copolymer (61k-*b*-57k and 26k-*b*-23k) single crystals grown at different solution crystallization temperatures (T_x).

(61k-*b*-57k) single crystals, $\tilde{\sigma}^{PS}$ varied from 8.3 to 12.3 by changing the T_x values from 20 to 37 °C. The $\tilde{\sigma}^{PS}$ values of PS-*b*-PEO (26k-*b*-23k) single crystals were determined to be between 7.7 and 12.9. The slopes of $1/d_{PEO}$ and T_x of these two PS-*b*-PEO mats are not significantly different because their $\tilde{\sigma}^{PS}$ values are all above the onset of overcrowding (>3.7).[38,39]

When the PEO single crystals are completely molten and tethered to the PS substrate surfaces, we need to know the reduced tethering densities of the PEO blocks ($\tilde{\sigma}^{PEO}$), which are different from those of $\tilde{\sigma}^{PS}$ values in the same PS-*b*-PEO mats. Although, the σ values for the PS and PEO blocks are identical because these two blocks share the same surface cross-section area. The R_g^{PEO} value can be deduced for the melt from the θ condition.[55] The $\tilde{\sigma}^{PEO}$ values were calculated and, along with all structural and property parameters of the series of PS-*b*-PEO mats, are summarized in Table 2. The $\tilde{\sigma}^{PEO}$ values are between 13 and 21 with almost all of them located in the highly stretched region (>14.3).[39]

***T_{rx}*-Dependent PEO Crystal Orientations under 1D Confinement with Various d_{PEO} and $\tilde{\sigma}^{PEO}$ Values.** Figure 5a−f shows typical WAXD patterns where the X-ray beam was directed along the *x*,*y*-plane (Figure 5a−c) and the *z*-direction (Figure 5d−f) of the PEO crystal mats (61k-*b*-57k) after recrystallization at three different T_{rx} values. (The *x*,*y*-plane and *z*-direction of the mats are shown in the inset of this Figure). Figure 5a,d shows typical 2D WAXD patterns when these mats were quenched in liquid N_2 for 10 min after melting at 67 °C for 4 min. Figure 5b,d shows 2D WAXD patterns after recrystallization at $T_{rx} = -20$ °C for 2 h. Figure 5c,f shows the patterns from $T_{rx} = 20$ °C, also recrystallized for 2 h via the self-seeding technique. The two WAXD patterns shown in Figure 5a,d are identical and exhibit two major isotropic diffraction rings with *d*-spacings of 0.463 and 0.39 nm. The inner ring with a *d*-spacing of 0.463 nm is indexed as the (120) diffraction, whereas the outside ring consists of overlapped (*hkl*) diffractions with a *d*-spacing of 0.39 nm. The appearance of these two identical isotropic ring patterns indicates that a random PEO

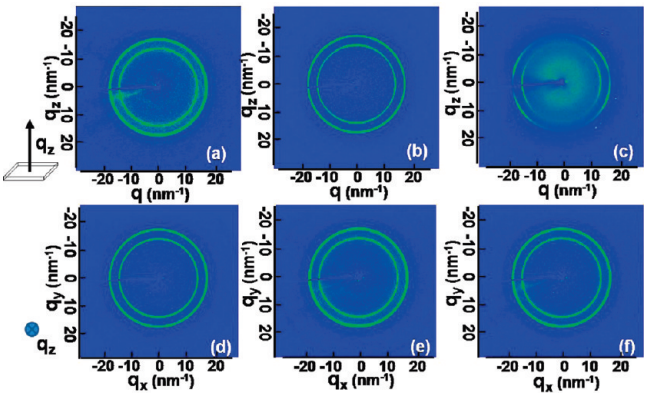

Figure 5. Three different 2D WAXD patterns, when the X-ray is along the edge direction of the mats (*x*,*y*-plane), commonly observed from the five PS-*b*-PEO diblock copolymer mats (61k-*b*-57k) with $\tilde{\sigma}^{PEO}$ values ranging from 13.6 to 20.2. The mats were quenched to different T_{rx} values for 1 h after melting the PEO single crystal layers at 67 °C for 4 min. (a) An isotropic ring pattern (random orientation) observed at extremely high supercooling after quenching to liquid nitrogen for 10 min. (b) A [4$\bar{2}$1] unaxial pattern (homogeneous orientation) observed at $T_{rx} = -20$ °C for 2 h. (c) A *c*-axis fiber pattern (homeotropic orientation) observed at $T_{rx} = 20$ °C via the self-seeding technique. (d,e,f) The corresponding isotropic ring patterns obtained when the X-ray is along the *z*-direction.

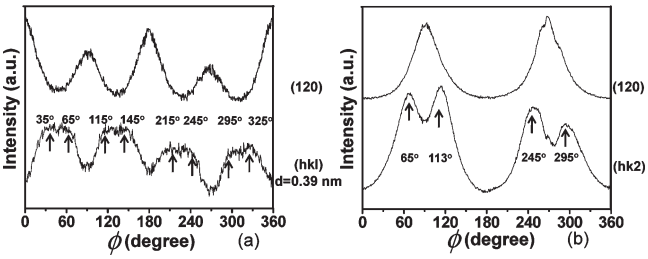

Figure 6. (a) Azimuthal scan profiles of Figure 5b of the [4$\bar{2}$1] zone pattern showing the two pairs of the (120) diffraction arcs at both equator and meridian (top) and four pairs of the overlapped diffraction arcs of ($\bar{1}$32), (032), (112), ($\bar{2}$12), ($\bar{1}$24), ($\bar{2}$04), and (004) (bottom). (b) Azimuthal scan profiles of Figure 5c of the *c*-axis fiber pattern showing only one pair of the (120) diffraction arcs at equator (top) and two pairs of the overlapped ($\bar{2}$12) and (112) diffraction arcs off the equator (bottom).

crystal orientation exists within the 1D confinement. It has been found that despite the variety in both the $\tilde{\sigma}^{PEO}$ and d_{PEO} values, such a deep quenching always leads to a formation of very small PEO crystals with their *c*-axis being randomly oriented, similar to our previous observations.[21,26,36,37] The deep quenching into the homogeneous nucleation region helps the creation of a very high primary nucleation density. The crystal formation thus completely relies on the nucleation and little on the growth to fill the 1D confined space. These crystals do not "feel" the confined PS layers.

Figure 5e,f shows isotropic 2D WAXD ring patterns for the PS-*b*-PEO mats recrystallized at $T_{rx} = -20$ and 20 °C, respectively, when the X-ray is directed along the PS layer normal direction (the *z*-direction). Again, these two WAXD patterns are identical and exhibit two major isotropic diffraction rings with *d*-spacings of 0.463 and 0.39 nm. The appearance of these two identical isotropic ring patterns taken at different T_{rx} values indicates that the PEO crystals always adopt a random orientation along the layer normal direction.

However, Figure 5b,c shows two different 2D WAXD patterns when the X-ray beam is along the direction that is perpendicular to the layer normal (the *x*,*y*-plane) at $T_{rx} = -20$

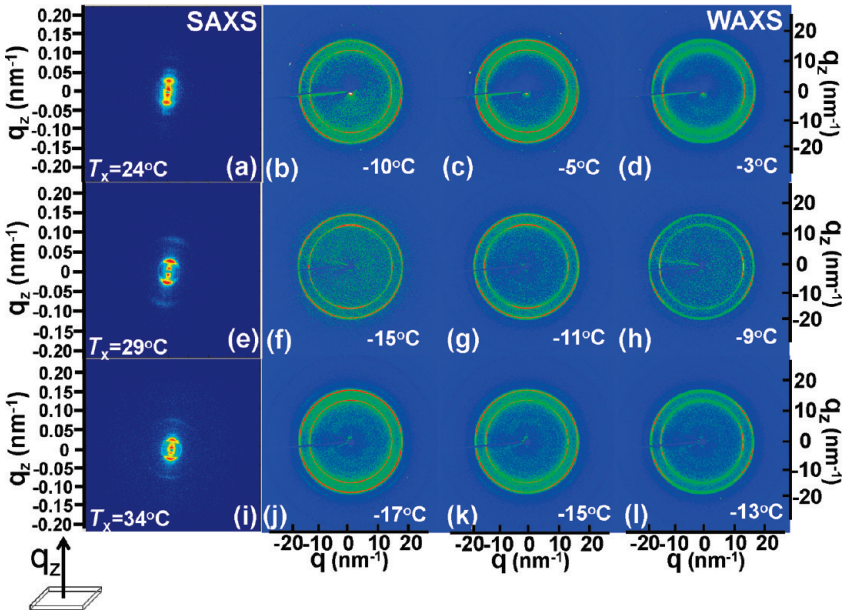

Figure 7. Set of simultaneous 2D X-ray patterns of three PS-*b*-PEO single crystal mats (61k-*b*-57k) grown at T_x = 24, 29, and 34 °C. 2D SAXS patterns with X-ray along the *x*,*y*-plane for the PS-*b*-PEO mats kept at T_{rx} = −10 °C for 1 h after melting the PEO single crystal at 67 °C as shown in (a) T_x = 24 °C, (e) T_x = 29 °C, and (i) T_x = 34 °C. The 2D WAXD patterns with the X-ray along the *x*,*y*-plane for PS-*b*-PEO mats kept at different T_{rx} as shown in (b−d) (T_x = 24 °C); in (f−h) (T_x = 29 °C); and in (j−l) (T_x = 34 °C). The T_{rx} values are inserted in these Figures.

and 20 °C, respectively. The PEO crystal orientations with respect to the PS layer normal at these two T_{rx} values can be quantitatively identified by the azimuthal profiles of Figure 5b,c on the basis of the PEO crystal unit cell geometry. They are shown in Figure 6a,b, correspondingly. The zero-angle ($\Phi = 0°$ in Figure 6) of the scans is set up at the meridian direction of those 2D WAXD patterns and increases along the clockwise (CW) direction.

Figure 5b exhibits one strong pair of (120) diffraction arcs (with a *d*-spacing of 0.463 nm) along the meridian and one weak pair of (120) diffraction arcs along the equator. As shown in Figure 6a, these two pairs of diffraction arcs with a *d*-spacing of 0.463 nm are located at 0, 90, 180, and 270°. The diffractions at 0 and 180° are stronger, whereas those at 90 and 270° are weaker. For the diffraction arcs with a *d*-spacing of 0.39 nm shown in Figure 5b, the azimuthal scan in Figure 6a shows four pairs of diffraction arcs at the azimuthal angles of 35, 65, 115, 145, 215, 245, 295, and 325°. They are the overlapped diffractions by combining two of the ($\bar{1}32$), (032), (112), ($\bar{2}12$), ($\bar{1}24$), ($\bar{2}04$), and (004) diffractions. On the basis of the crystallography of PEO, this diffraction pattern can be explained by using a [$4\bar{2}1$] uniaxial pattern with the [$4\bar{2}1$] zone being along the meridian direction.[21,56,57] It is demonstrated that the *c*-axis of the PEO crystals possesses a homogeneous orientation in the confined layers. (The *c*-axis of the crystals is perpendicular to the PS layer normal.)

The azimuthal scan profiles with *d*-spacings of 0.463 and 0.39 nm (the (120) and overlapped diffractions) of Figure 5c are shown in Figure 6b. It is evident that only one pair of the (120) diffraction arcs is located on the equator, whereas two pairs of the overlapped diffractions are at 65 and 245° and 113 and 295° away from the meridian. This WAXD pattern indicates a *c*-axis fiber pattern of PEO crystals and demonstrates that the *c*-axis of the recrystallized PEO crystals is oriented approximately parallel to the layer normal of the mats, as analyzed in our previous publications.[21,26]

Two distinct WAXD patterns shown in Figure 5b,c thus represent the fact that at low T_{rx} values, the *c*-axis of the PEO crystals is oriented perpendicular to the PS layer normal (the homogeneous orientation), whereas at high T_{rx} values, the *c*-axis orientation of the PEO crystals changes to become homeotropic (parallel to the PS layer normal). This qualitative, universal trend in the *c*-axis orientation change in these PEO crystals with increased T_{rx} under 1D confinements having fixed d_{PEO} and $\tilde{\sigma}^{PEO}$ values has been found.[37] However, detailed investigations concerning the role of d_{PEO} and $\tilde{\sigma}^{PEO}$ on the *c*-axis orientation change has not been explored.

Figure 7a−l shows a set of simultaneous 2D SAXS and WAXD patterns of three different PS-*b*-PEO (61k-*b*-57k) mats recrystallized in the T_{rx} ranging from −20 to 20 °C. These were taken with the X-ray along the *x*,*y*-plane (inset of the Figure) after the single crystals were grown in solution at different T_x values, as shown in this Figure. Figure 7a,e,i, which corresponds to T_x = 24, 29, and 34 °C, respectively, shows highly oriented 2D SAXS patterns. The shape and locations of the scattering arcs in these three 2D SAXS patterns remain identical after melting the mats at 67 °C for 4 min and recrystallizing at −10 °C. This indicates that layered confinements are preserved during the recrystallization process of the PEO blocks. Figure 7b,d,f,h,j,l shows 2D WAXD patterns obtained from this set of mats after melting and recrystallizing at specific T_{rx} values identified in the Figure. The d_{PEO} and $\tilde{\sigma}^{PEO}$ values of these three mats are $\tilde{\sigma}^{PEO}$ = 15.4, 16.4, and 18.4 and d_{PEO} = 10.4, 11.4, and 12.7 nm, respectively (Table 2). For the PS-*b*-PEO single crystal mats grown at T_x = 24 °C ($\tilde{\sigma}^{PEO}$ = 15.4 and d_{PEO} = 10.4 nm), it is evident that the *c*-axis orientation change of the PEO crystals occurs at T_{rx} = −4 °C, and it is defined as the onset temperature of the *c*-axis orientation change (T_{onset}). Furthermore, it is observed that T_{onset} is −10 and −16 °C for the PS-*b*-PEO mats prepared at T_x = 29 ($\tilde{\sigma}^{PEO}$ = 16.4 and d_{PEO} = 11.4 nm) and 34 °C ($\tilde{\sigma}^{PEO}$ = 18.4 and d_{PEO} = 12.7 nm), respectively. In the case of the entire set of five PS-*b*-PEO (61k-*b*-57k) mats, the T_{onset} values are identified at different T_{rx} values. Therefore, the T_{onset} value must be associated with the variations of d_{PEO} and $\tilde{\sigma}^{PEO}$.

Figure 8 shows the relationship of the *c*-axis orientation to the PS layer normal at different T_{rx} values for the PS-*b*-PEO (61k-*b*-57k) mats prepared at five T_x values. The main

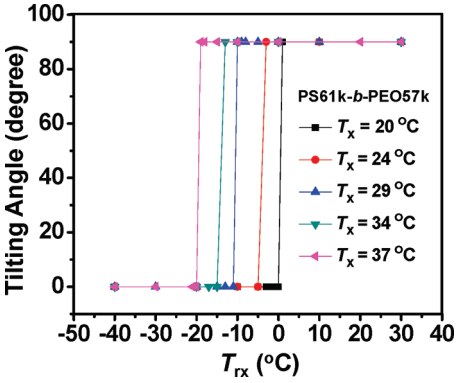

Figure 8. Relationship of the *c*-axis orientation (angles with respect to the glassy PS layer plane) with the T_{rx} values for these five PS-*b*-PEO mats (61k-*b*-57k) grown at solution crystallization temperatures ranging from 20 to 37 °C.

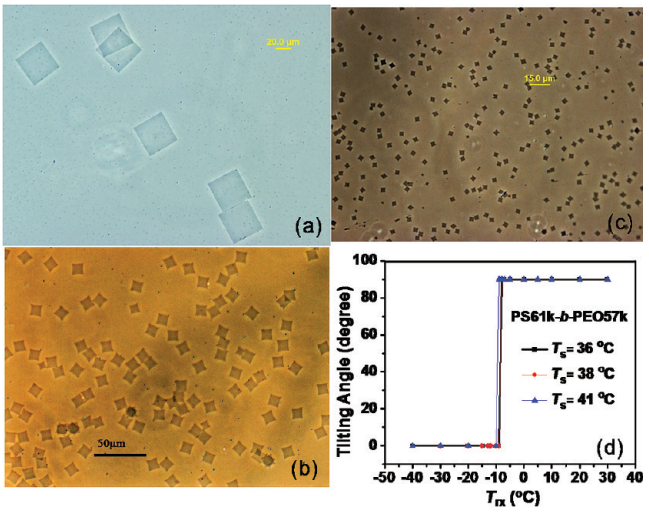

Figure 9. Phase contrast optical microscopy (PCOM) images of PS-*b*-PEO diblock copolymer single crystals (61k-*b*-57k) grown at T_x = 29 °C from three different self-seeding temperatures, T_s, of (a) 41, (b) 38, and (c) 36 °C. (d) The onset temperatures of the crystal orientation change for the three PS-*b*-PEO lamellar mats having different confined volumes.

feature to be focused on is the T_{rx} value where the sharp change from homogeneous to homeotropic orientation takes place in the recrystallized PEO crystals (T_{onset}). It is evident that T_{onset} is significantly different and shifts from −20 to 0 °C by increasing the T_x from 20 to 37 °C, which corresponds to increases in d_{PEO} and $\tilde{\sigma}^{PEO}$ for a single diblock copolymer single crystal sample. Therefore, we conclude that changes of both d_{PEO} and $\tilde{\sigma}^{PEO}$ can vary the T_{onset} value. The question is whether we can find quantitative relationships of the T_{onset} with the d_{PEO} and $\tilde{\sigma}^{PEO}$ values and whether one parameter dominates over the other.

There may be another possible factor to influence the T_{onset} value in these PS-*b*-PEO mats that needs to be carefully examined, the overall confined volume of the single crystals (in cubic micrometers). Note that in the PS-*b*-PEO single crystals the ratio between the lateral dimension and the crystal thickness is >4000. In one of our previous publications,[37] it was concluded that there is a matching of the T_{onset} with the starting temperature where homogeneous nucleation takes place in PEO droplet experiments,[59−62] which were initially devised by Vonnegut in 1948.[63] The reason might be attributed to these two systems having similar confined volumes on the cubic micrometer level. In Figure 1a−d, the sizes of these PS-*b*-PEO single crystals grown at different T_x values are not absolutely identical and result in the existence of a difference in lamellar confined volume among these PS-*b*-PEO mats. Does the shift of the T_{onset} shown in Figure 8 merely attribute to the variation of confined volume? To isolate and understand this confined volume effect, we investigated a series of single crystal mats having fixed d_{PEO} and $\tilde{\sigma}^{PEO}$ values but varying lateral sizes to change the confined volume.

Figure 9a−c shows three PCOM micrographs of PS-*b*-PEO (61k-*b*-57k) single crystals grown at T_x = 29 °C but from three different self-seeding temperatures (T_s = 41, 38, and 36 °C). With increasing T_s, the surviving population of the PEO nuclei decreases, which results in crystals with a larger lateral size. This method was, therefore, used to control the confined volume of single crystals grown from these nuclei while keeping their d_{PEO} and $\tilde{\sigma}^{PEO}$ values constant at T_x = 29 °C. These three Figures show that the lateral lengths of the single crystals are 50, 10, and 3 μm. They are equivalent to confined volumes for the PEO single crystal of 28.5, 1.14, and 0.1 μm^3, respectively. (The d_{PEO} in the three cases is 11.4 nm.) Figure 9d presents the T_{rx} dependence of the *c*-axis orientation change of the recrystallized PEO crystals for these three PS-*b*-PEO mats (61k-*b*-57k) having different confined sizes on the cubic micrometer level. It is evident that these T_{onset} values are located at a temperature between −9 and −10 °C, even though the difference of the confined volume among the three lamellar mats reaches 2 orders of magnitude. The observation that the T_{onset} values are more or less independent of the confined volumes when the d_{PEO} and $\tilde{\sigma}^{PEO}$ values are fixed truly excludes the confined volume effect as the cause of the shift in T_{onset} values.

Role of d_{PEO} and $\tilde{\sigma}^{PEO}$ on the T_{rx}-Dependent Crystal Orientation Change. To confirm that the shift of T_{onset} with increasing d_{PEO} and $\tilde{\sigma}^{PEO}$ values is a universal trend, the T_{rx}-dependent PEO crystal orientations for another symmetric PS-*b*-PEO sample having different d_{PEO} and $\tilde{\sigma}^{PEO}$ values were examined carefully. Figure 10 presents the T_{rx}-dependent *c*-axis orientation for the PS-*b*-PEO (26k-*b*-23k) mat samples, as determined by using methods identical to those listed above for the PS-*b*-PEO (61k-*b*-57k) sample. It was found that the T_{rx}-dependent *c*-axis orientation changes of the PEO crystals for these two symmetric PS-*b*-PEO cases (Figures 8 and 10) are highly similar, including the same T_{rx} region within which the different T_{onset} values were located (−20 to 0 °C). They also have similar d_{PEO} and $\tilde{\sigma}^{PEO}$ values at a constant T_x value. It is interesting that the T_{onset} values can cover 20 °C by varying the d_{PEO} and $\tilde{\sigma}^{PEO}$ values only slightly. These T_{onset} values for ten different PS-*b*-PEO mats having similar confined volume are summarized in Table 2. An apparent observation of this study indicates that the T_{onset} value in the PS-*b*-PEO mats matches only coincidently with the starting temperature of homogeneous nucleation of PEO homopolymer in the droplet experiments. Although both cases have similar confined dimension, the latter (droplets) is represented only by a confined volume effect, and the former (PS-*b*-PEO mats) has been demonstrated to be affected by at least two other structural parameters, d_{PEO} and $\tilde{\sigma}^{PEO}$.

A qualitative understanding of the effect of d_{PEO} and $\tilde{\sigma}^{PEO}$ on the *c*-axis orientation change for these mats after recrystallization at different T_{rx} values was determined from these two sets of data. Specifically, the larger $\tilde{\sigma}^{PEO}$ value may help the *c*-axis in the PEO crystals to adopt the homeotropic orientation (parallel to the PS layer normal) because of the fact that more PEO segmental stretching near the PS

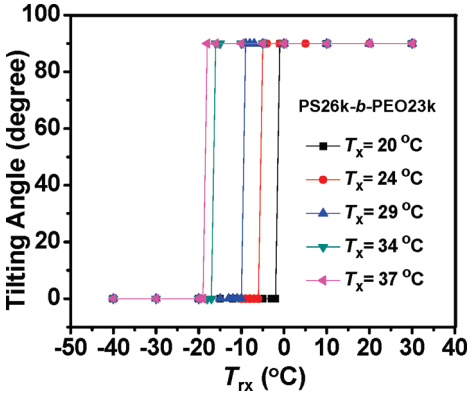

Figure 10. Relationship of the *c*-axis orientation with the T_{rx} values for PS-*b*-PEO mats (26k-*b*-23k) grown at solution crystallization temperatures ranging from 20 to 37 °C.

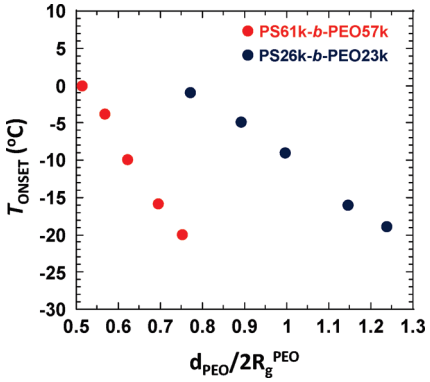

Figure 11. Relationship of the $d_{PEO}/2R_g^{PEO}$ and T_{onset} values in two symmetric PS-*b*-PEO single crystal mats collected at different crystallization temperatures in dilute solution ranging from 20 to 37 °C.

interface can be achieved. The decrease in d_{PEO} may induce both the anisotropic chain conformation and anisotropic density fluctuation in the PEO melt, specifically when the d_{PEO} value is smaller than the value of twice the PEO radius of gyration ($2R_g^{PEO}$). This may lead to an enhancement in the formation of the homogeneous orientation (perpendicular to the PS layer normal) of the *c*-axis in the PEO crystals. As seen in Table 2, it is clearly shown that both the d_{PEO} value along the PS layer normal and the $\tilde{\sigma}^{PEO}$ values increase with increasing T_x.

Quantitatively, the degree of anisotropy of the PEO melt under 1D confinement can be defined as a ratio between d_{PEO} and $2R_g^{PEO}$ ($d_{PEO}/2R_g^{PEO}$) in the melt. The R_g^{PEO} values in these two PS-*b*-PEO samples (26k-*b*-23k and 61k-*b*-57k) can be easily calculated to be 5.8 and 9.1 nm, respectively.[55] The d_{PEO} values in Table 2 are smaller than $2R_g^{PEO}$. This ratio gradually increases when the T_x value increases from 20 to 37 °C, indicating that the degree of anisotropy of the PEO melt decreases with increasing T_x. Therefore, at a fixed $d_{PEO}/2R_g^{PEO}$ value for each PS-*b*-PEO mat sample, there must be a corresponding T_{onset} value below which the *c*-axis orientation becomes homogeneous.

Figure 11 plots the relationships between T_{onset} and $d_{PEO}/2R_g^{PEO}$ for both sets of crystal mats. It is evident that two linear relationships can be observed for both sets of mats. This indicates that with smaller d_{PEO} values, the change from homogeneous to homeotropic orientation takes place at a higher T_{onset} temperature. From the viewpoint of critical nucleus formation, the ability of the nucleus for parallel or perpendicular directions to overcome the nucleation barrier relies on the density fluctuation along these two directions.

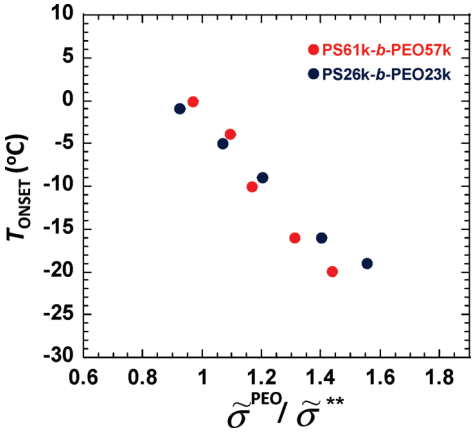

Figure 12. Relationship of the $\tilde{\sigma}^{PEO}/\tilde{\sigma}^{**}$ ($\tilde{\sigma}^{**} = 14$) and T_{onset} in two symmetric PS-*b*-PEO single crystal mats collected at different crystallization temperatures in dilute solution ranging from 20 to 37 °C.

The homogeneous nucleation mechanism has been recently examined theoretically by linearized time-dependent Ginzburg−Landau equations.[64] Differentiating the ability of forming critical nuclei for both parallel and perpendicular directions with respect to the PS layer normal relies on $d_{PEO}/2R_g^{PEO}$. A significant increase in the anisotropies of the overall chain conformation and the density fluctuation by decreasing confined dimension could cause the homogeneously oriented PEO crystals to form at a higher T_{rx}.

The effect of $\tilde{\sigma}^{PEO}$ on the T_{onset} value lies on the orientation of the PEO segments near the junction between the PS and PEO blocks. In fact, the $\tilde{\sigma}^{PEO}$ values listed in Table 2 are in the highly stretched brush regime,[39] indicating that the tethered PEO segment conformations in the melt near the PS interface in all of these PS-*b*-PEO mats should be highly stretched and oriented, to a certain degree, along the PS layer normal. Assuming that there is no restriction of the PEO layer thickness, a higher $\tilde{\sigma}^{PEO}$ value causes further stretching of these PEO segmental conformations and may promote preferential orientation and assist in the formation of the homeotropically oriented PEO crystals. Such an effect has been recently examined theoretically by Monte Carlo simulation experiments.[65]

However, this molecular argument of the segmental orientation near the PS interface in the current case is also subject to the influence of the PEO layer thickness. The overall PEO chain conformational shape may not coincide with the segmental orientation near the PS interface. Therefore, a combination of the effects of both d_{PEO} and $\tilde{\sigma}^{PEO}$ on the T_{onset} values needs to be taken into account. It is known that tethered chains undergo a transition from the overcrowded regime to the highly stretched regime at $\tilde{\sigma}^{**}$ of ~14.[39] If we assume that this value for the PEO block is 14 and use the quantity of $\tilde{\sigma}^{PEO}/\tilde{\sigma}^{**}$ to represent how far the overall conformation of the tethered chain deviates from the highly stretched one, then we can plot the relationship of $\tilde{\sigma}^{PEO}/\tilde{\sigma}^{**}$ with the T_{onset} values. This is shown in Figure 12. Again, two linear relationships can be found, indicating that the smaller $\tilde{\sigma}^{PEO}$ value corresponds to a higher T_{onset} value. Microscopically, the smaller $\tilde{\sigma}^{PEO}$ value thus generates a less-oriented segmental orientation near the PS interface and causes the homeotropic orientation in PEO crystals to occur at a higher T_{rx}. The affect of $\tilde{\sigma}^{PEO}$ on the T_{onset} and *c*-axis orientation appears to be more universal for PEO than the $d_{PEO}/2R_g^{PEO}$. The T_{onset} value for a given $\tilde{\sigma}^{PEO}$ is nearly identical for both PS-*b*-PEO samples; whereas, $d_{PEO}/2R_g^{PEO}$ (i.e., around 1.0) gives drastically different results for the two

samples possibly because of the difference between these two radii of gyration of the PEO blocks in the two samples. To obtain a master curve of these two linear relationships in Figure 11, we may require a reduced quantity designed for the radii of gyration. The overall effect is still a combination of the two because they are not mutually exclusive; however, the $\tilde{\sigma}^{PEO}$ value might have more influence because of the apparent universality for these samples.

Conclusions

In summary, this study showed for the first time that the PEO crystal orientation change, from homogeneous to homeotropic, of the *c*-axis with respect to the PS layer normal in two symmetric PS-*b*-PEO single crystal mat samples is not at a constant temperature but can shift within a wide temperature region of over 20 °C. Although it was found in the past that these changes coincidently happen with the starting temperature of the homogeneous nucleation of PEO, it is evident now that the orientation changes in this 1D confined environment possess their own determining factors: the PEO layer thickness, d_{PEO}, and its reduced tethering density, $\tilde{\sigma}^{PEO}$. Microscopically, we introduced two parameters: $d_{PEO}/2R_g^{PEO}$, which represents how thin the PEO layer thickness is compared with twice the radius of gyration of the PEO chains, and $\tilde{\sigma}^{PEO}/\tilde{\sigma}^{**}$ ($\tilde{\sigma}^{**} = 14$), which represents how crowded the PEO chains are on the PS layer compared with the highly stretched conformation. With an increase in the d_{PEO}, the onset temperature of the crystal orientation change, T_{onset}, decreases. This indicates that the confined layer thickness leads to a compression of the overall PEO chain conformation, and thus, it favors the *c*-axis of the PEO crystals adopting the homogeneous orientation. On the other hand, the increase in $\tilde{\sigma}^{PEO}$ causes a decrease in the T_{onset} value because the segmental orientation of PEO chains parallel to the layer normal near the PS interface facilitates the homeotropic orientation of the *c*-axis of the PEO crystals. Quantitative analysis indicates that both parameters are combined to affect the T_{onset} value, leading to the onset temperature of the *c*-axis orientation change exhibiting a variation of over 20 °C in temperature.

Acknowledgment. This work was supported by NSF (DMR-0516602 and DMR-0906898). We also acknowledge the Perkin-Elmer Co. for providing a Diamond DSC instrument for our laboratory.

References and Notes

(1) Hamley, I. W. *The Physics of Block Copolymers*; Oxford University Press: New York, 1998.
(2) Cohen, R. E.; Cheng, P. L.; Douzinas, K. C.; Kofinas, P.; Berney, C. V. *Macromolecules* **1990**, *23*, 324.
(3) Douzinas, K. C.; Cohen, R. E. *Macromolecules* **1992**, *25*, 5030.
(4) Sakurai, K.; MacKnight, W. J.; Lohse, D. J.; Schulz, D. N.; Sissano, J. A. *Macromolecules* **1993**, *26*, 3236.
(5) Cohen, R, E.; Bellare, A.; Drzewinski, M. A. *Macromolecules* **1994**, *27*, 2321.
(6) Khandpur, A. K.; Macosko, C. W.; Bates, F. S. *J. Polym. Sci., Polym. Phys. Ed.* **1995**, *33*, 247.
(7) Hamley, I. W.; Fairclough, J. P. A.; Ryan, A. J.; Bates, F. S.; Towns-Andrews, E. *Polymer* **1996**, *37*, 4425.
(8) Zhao, J.; Majumdar, B.; Schulz, M. F.; Bates, F. S.; Almdal, K.; Mortensen, K.; Hajduk, D. A.; Gruner, S. M. *Macromolecules* **1996**, *29*, 1204.
(9) Liu, L. Z.; Yeh, F.; Chu, B. *Macromolecules* **1996**, *29*, 5336.
(10) Hamley, I. W.; Fairclough, J. P. A.; Terrill, N. J.; Ryan, A. J.; Lipic, P. M.; Bates, F. S.; Towns-Andrews, E. *Macromolecules* **1996**, *29*, 8835.
(11) Park, C.; De Rosa, C.; Fetters, L. J.; Thomas, E. L. *Macromolecules* **2000**, *33*, 7931.
(12) Loo, Y. L.; Register, R. A.; Ryan, A. J. *Phys. Rev. Lett.* **2000**, *84*, 4120.
(13) Loo, Y. L.; Register, R. A.; Adamson, D. H. *Macromolecules* **2000**, *33*, 8361.
(14) Loo, Y. L.; Register, R. A.; Ryan, A. J. *Macromolecules* **2002**, *35*, 2365.
(15) Quiram, D. J.; Register, R. A.; Marchand, G. R. *Macromolecules* **1997**, *30*, 4551.
(16) Quiram, D. J.; Register, R. A.; Marchand, G. R.; Ryan, A. J. *Macromolecules* **1997**, *30*, 8338.
(17) Quiram, D. J.; Register, R. A.; Marchand, G. R.; Adamson, D. H. *Macromolecules* **1998**, *31*, 4891.
(18) Xu, J.-T.; Fairclough, J. P. A.; Mai, S.-M.; Ryan, A. J.; Chaibundit, C. *Macromolecules* **2002**, *35*, 6937.
(19) Xu, J.-T.; Fairclough, J. P. A.; Mai, S.-M.; Chaibundit, C.; Mingvanish, M.; Booth, C.; Ryan, A. J. *Polymer* **2003**, *44*, 6843.
(20) Zhu, L.; Chen, Y.; Zhang, A.; Calhoun, B. H.; Chun, M.; Quirk, R. P.; Cheng, S. Z. D.; Hsiao, B. S.; Yeh, F.; Hashimoto, T. *Phys. Rev. B* **1999**, *60*, 10022.
(21) Zhu, L.; Cheng, S. Z. D.; Calhoun, B. H.; Ge, Q.; Quirk, R. P.; Thomas, E. L.; Hsiao, B. S.; Yeh, F.; Lotz, B. *J. Am. Chem. Soc.* **2000**, *122*, 5957.
(22) Zhu, L.; Calhoun, B. H.; Chun, M.; Quirk, R. P.; Cheng, S. Z. D.; Thomas, E. L.; Lotz, B.; Hsiao, B. S.; Yeh, F.; Liu, L. *Macromolecules* **2001**, *34*, 1244.
(23) Huang, P.; Zhu, L.; Cheng, S. Z. D.; Ge, Q.; Quirk, R. P.; Thomas, E. L.; Lotz, B.; Hsiao, B. S.; Liu, L.; Yeh, F. *Macromolecules* **2001**, *34*, 6649.
(24) Zhu, L.; Cheng, S. Z. D.; Huang, P.; Ge, Q.; Quirk, R. P.; Thomas, E. L.; Lotz, B.; Hsiao, B. S.; Yeh, F.; Liu, L. *Adv. Mater.* **2002**, *14*, 31.
(25) Zhu, L.; Huang, P.; Chen, W. Y.; Ge, Q.; Quirk, R. P.; Cheng, S. Z. D.; Thomas, E. L.; Lotz, B.; Hsiao, B. S.; Yeh, F.; Liu, L. *Macromolecules* **2002**, *35*, 3553.
(26) Huang, P.; Zhu, L.; Guo, Y.; Ge, Q.; Jing, A. J.; Chen, W. Y.; Quirk, R. P.; Cheng, S. Z. D.; Thomas, E. L.; Lotz, B.; Hsiao, B. S.; Avila- Orta, C. A.; Sics, I. *Macromolecules* **2004**, *37*, 3689.
(27) Huang, P.; Guo, Y.; Quirk, R. P.; Ruan, J.; Lotz, B.; Thomas, E. L.; Hsiao, B. S.; Avila-Orta, C. A.; Sics, I.; Cheng, S. Z. D. *Polymer* **2006**, *47*, 5457.
(28) Huang, P.; Zheng, J. X.; Leng, S.; Van Horn, R. M.; Jeong, K. U.; Guo, Y.; Quirk, R. P.; Cheng, S. Z. D.; Lotz, B.; Thomas, E. L.; Hsiao, B. S. *Macromolecules* **2007**, *40*, 526.
(29) Sun, Y. S.; Chung, T. M.; Li, Y. J.; Ho, R. M.; Ko, B. T.; Jeng, U. S.; Lotz, B. *Macromolecules* **2006**, *39*, 5782.
(30) Sun, Y. S.; Chung, T. M.; Li, Y. J.; Ho, R. M.; Ko, B. T.; Jeng, U. S.; Lotz, B. *Macromolecules* **2007**, *40*, 6781.
(31) Zhu, L.; Cheng, S. Z. D.; Calhoun, B. H.; Ge, Q.; Quirk, R. P.; Thomas, E. L.; Hsiao, B. S.; Yeh, F.; Lotz, B. *Polymer* **2001**, *42*, 5829.
(32) Cheng, S. Z. D.; Barley, J. S.; Zhang, A.; Habenschuss, A.; Zschack, P. R. *Macromolecules* **1992**, *25*, 1453.
(33) Wunderlich, B. Chapter 4. In *Macromolecular Physics: Crystal Structure, Morphology, Defects*; Academic Press: New York, 1973; Vol. *I*.
(34) Gido, S. P.; Thomas, E. L. *Macromolecules* **1994**, *27*, 6137.
(35) Marencic, A. P.; Wu, M. W.; Register, R. A.; Chaikin, P. M. *Macromolecules* **2007**, *40*, 7299.
(36) Hsiao, M.-S.; Chen, W. Y.; Zheng, J. X.; Van Horn, R. M.; Quirk, R. P.; Ivanov, D. A.; Thomas, E. L.; Lotz, B.; Cheng, S. Z. D. *Macromolecules* **2008**, *41*, 4794.
(37) Hsiao, M.-S.; Zheng, J. X.; Leng, S. W.; Van Horn, R. M.; Quirk, R. P.; Thomas, E. L.; Chen, H.-L.; Hsiao, B. S.; Rong, L.; Lotz, B.; Cheng, S. Z. D. *Macromolecules* **2008**, *41*, 8114.
(38) Chen, W. Y.; Zheng, J. X.; Cheng, S. Z. D.; Li, C. Y.; Huang, P.; Zhu, L.; Xiong, H.; Ge, Q.; Guo, Y.; Quirk, R. P.; Lotz, B.; Deng, L.; Wu, C.; Thomas, E. L. *Phys. Rev. Lett.* **2004**, *93*, 028301.
(39) Zheng, J. X.; Xiong, H.; Chen, W. Y.; Lee, K.; Van Horn, R. M.; Quirk, R. P.; Lotz, B.; Thomas, E. L.; Shi, A.-C.; Cheng, S. Z. D. *Macromolecules* **2006**, *39*, 641.
(40) Quirk, R. P.; Kim, J.; Kausch, C.; Chun, M. S. *Polym. Int.* **1996**, *39*, 3.
(41) Lotz, B.; Kovacs, A. J.; Bassett, G. A.; Keller, A. *Kolloid Z. Z. Polym.* **1966**, *209*, 115.
(42) Chen, W. Y.; Li, C. Y.; Zheng, J. X.; Huang, P.; Zhu, L.; Ge, Q.; Quirk, R. P.; Lotz, B.; Deng, L.; Wu, C.; Thomas, E. L.; Cheng, S. Z. D. *Macromolecules* **2004**, *37*, 5292.
(43) Lotz, B.; Kovacs, A. J. *Kolloid Z. Z. Polym.* **1966**, *209*, 97.
(44) Organ, S. J.; Keller, A. *J. Mater. Sci.* **1985**, *20*, 1571.
(45) Organ, S. J.; Keller, A. *J. Mater. Sci.* **1985**, *20*, 1602.
(46) Lotz, B.; Kovacs, A. J. *Kolloid Z. Z. Polym.* **1966**, *209*, 97.
(47) Cheng, S. Z. D.; Wunderlich, B. *J. Polym. Sci., Polym Phys Ed.* **1986**, *24*, 577.

(48) Porod, G. *Kolloid-Z*. **1951**, *124*, 83.
(49) Porod, G. *Kolloid-Z*. **1952**, *125*, 51.
(50) Porod, G. *Kolloid-Z*. **1952**, *125*, 108.
(51) Ruland, W. *J. Appl. Crystallogr*. **1971**, *4*, 70.
(52) Strobl, G. R.; Schneider, M. *J. Polym. Sci., Polym. Phys. Ed.* **1980**, *18*, 1343.
(53) Cheng, S. Z. D. *Phase Transitions in Polymers: The Role of Metastable States*; Elsevier: Amsterdam, 2008.
(54) Vonk, C. G. *J. Appl. Crystallogr*. **1978**, *11*, 541.
(55) Rubinstein, M.; Colby, R. H. Chapter 1. In *Polymer Physics*, Oxford University Press: New York, 2004.
(56) Alexander, L. E. *X-ray Diffraction Methods in Polymer Science*; Wiley-Interscience: New York, 1969.
(57) Takahashi, Y.; Tadokoro, H. *Macromolecules* **1973**, *6*, 672.
(58) Tadokoro, H.; Chatani, Y.; Yoshihara, T.; Tahara, S.; Murahashi, S. *Makromol. Chem*. **1964**, *73*, 109.
(59) Koutsky, J. A.; Walton, A. G.; Baer, E. *J. Appl. Phys*. **1967**, *38*, 1832.
(60) Müller, A. J.; Balsamo, V.; Arnal, M. L. *Adv. Polym. Sci*. **2005**, *190*, 1.
(61) Massa, M. V.; Carvalho, J. L.; Dalnoki-Veress, K. *Eur. Phys. J. E* **2003**, *12*, 111.
(62) Massa, M. V.; Dalnoki-Veress, K. *Phys. Rev. Lett*. **2004**, *92*, 255509.
(63) Vonnegut, B. *J. Colloid Sci*. **1948**, *3*, 563.
(64) Tan, H.; Miao, B.; Yan, D. *J. Chem. Phys*. **2003**, *119*, 2886.
(65) Hu, W.; Frenkel, D. *Faraday Discuss*. **2005**, *128*, 253.